RSC Advances

PAPER

View Article Online
View Journal | View Issue

Cite this: *RSC Adv.*, 2022, **12**, 34200

New family of layered N-based cathode materials for sodium-ion batteries†

Yundan Jiang, Wangping Xu, Wei Zhao * and Juexian Cao*

The cathode materials of sodium-ion batteries (SIBs) have received considerable attention not only because of their abundant natural reserves and chemical properties similar to those of lithium-ion batteries but also their great potential in energy storage and conversion technologies. However, their low capacity and high diffusion barrier remain unsolved problems. In this work, we systematically studied the theoretical capacity and sodium ion diffusion barrier in a new family of layered transition metal compounds, named MX_2 (M = Ti, V, Cr, Mn, and Fe; X = C, N, and O), as the cathode materials of SIBs. The results indicate that all 2H-phase MX_2 materials possess a high theoretical capacity of over 300 mA h g^{-1}. Moreover, it is found that the 2H-phase CrN_2 exhibits a desirable sodium ion diffusion barrier, indicating high mobility of sodium ions. In addition, the layered CrN_2 has a remarkable voltage window (3.1–3.8 V) and outstanding electrochemical performance arising from the charge transfer between Na and N atoms, which is induced by the large electronegativity of nitrogen. Our research provides a promising candidate for application in SIB cathode materials in the future.

Received 8th October 2022
Accepted 24th November 2022

DOI: 10.1039/d2ra06336k

rsc.li/rsc-advances

1. Introduction

Sodium-ion batteries (SIBs) have increasingly received attention not only because of their similar intercalation properties to lithium-ion batteries but also the wide distribution and low cost of sodium.[1] Sodium-ion batteries exhibit remarkable electrochemical performance, including good cycle stability and high rate performance, which endow them with great application potential in the field of electric vehicles and large-scale energy storage.[2] Cathode materials, as an important component of the sodium-ion battery, play a key role in improving battery performance and bringing down battery costs.[3]

High-performance cathode material for SIBs calls for not only a high theoretical capacity but also good cycle stability and high-rate performance.[4] Following the success of cathode materials of lithium-ion batteries, various cathode materials for SIBs have been reported, such as layered transition metal oxides, polyanionic compounds, Prussian blue analogs and organic materials.[5] It is found that layered metal oxides, such as $NaMO_2$ (M = Co, Mn, Fe),[6–8] have high theoretical capacity. However, the multi-phase transition is easily induced in layered metal oxide during the charge and discharge processes, which badly hinders the diffusion of sodium ions.[9,10] On the contrary, polyanionic compounds, like $NaMPO_4$ (M = Mn, Fe, Co, Ni),[11,12] have excellent cycle stability and high rate performance due to their fast sodium ion diffusion rates. But the heavy polyanions lead to a limited specific capacity.[13] Experimentally, the electrochemical performance of the electrode material has been improved by ion doping[9,14] and morphology control,[10,15] while their intrinsically low specific capacity and sodium ion diffusion properties have not been enhanced.

Recently, transition metal dichalcogenides (TMDs), such as MX_2 (M = Mo, W, Nb, Ta; X = S, Se),[16–18] have attracted considerable attention due to their high theoretical capacity and graphite-like layered structure, which facilitates the intercalation and de-intercalation of sodium ions in the interlayer of TMDs.[19,20] However, the phase transition and poor conductivity of TMDs impede their practical applications.[21] Therefore, it is desirable to design a high-performance cathode material featuring high theoretical capacity, long cycle life and high rate performance. Some two-dimensional materials, such as monolayer ScO_2 (ref. 22), BP_2 (ref. 23) and V_2O_5,[24,25] have a large specific surface area and an unrestricted sodium diffusion path, which make their excellent sodium storage capacity and diffusion properties.[26] However, their generally poor conductive properties hinder the transmission of electrons. Furthermore, it is difficult for single-layer materials to achieve practical

Department of Physics & Hunan Institute of Advanced Sensing and Information Technology, Xiangtan University, Xiangtan, 411105, China. E-mail: zhaowei@xtu.edu.cn; jxcao@xtu.edu.cn

† Electronic supplementary information (ESI) available: The fully optimized structures of all 1T- and 2H-phase MX_2 are shown in Fig. S1. The energy profile of sodium diffusion along the diffusion path in MX_2 (M = Ti, V, Mn and Fe; X = C, N and O) is shown in Fig. S2. The intercalation energy for Na intercalated in 2H-phase MX_2 is shown in Fig. S3. The most stable configurations of Na_xCrN_2 (x = 0–1) at different sodium concentrations are shown in Fig. S4. Fig. S5 shows the differential charge density of $NaCrN_2$. Table S1 gives the lattice parameters of all MX_2 systems. Table S2 gives a direct comparison of cell parameters between our predicted 2H-VN_2 and theoretically reported H-phase VN_2 monolayer. Table S3 gives the relaxed atomic positions of 2H-phase CrN_2. See DOI: https://doi.org/10.1039/d2ra06336k

applications in sodium-ion batteries. Recently, transition metal nitrides have been fabricated experimentally,[27–29] and they have also received increasing attention theoretically.[30] It is shown that N-based compounds have ultra-high hardness and good electrical conductivity, especially N-based TMDs-like layered transition metal compounds with a large interlayer spacing, which is conducive to the diffusion of large sodium ions. Two-dimensional transition metal N-based materials (*i.e.* MoN_2 (ref. 31), VN_2 (ref. 32), and Zr_2N[33]) have both high capacity and extremely fast Na diffusion performance, besides, they usually exhibit metallic features and boast good electronic conductivity, suggesting that they can serve as potential cathode SIBs materials.

Thanks to their excellent electrochemical performance, including suitable sodium ion diffusion rate, extraordinary theoretical capacity, stable structural framework, and good electronic conductivity, layered N-based TMDs-like bulk materials hold a great potential to become excellent cathode materials of SIBs. In this work, we have systematically studied the theoretical capacity and sodium ion diffusion barrier in layered bulk transition metal compounds named MX_2 (M = Ti, V, Cr, Mn and Fe; X = C, N and O). Our results indicated that most of them possess high theoretical capacity and low sodium ion diffusion barrier. 2H-Phase bulk CrN_2 in particular shows the lowest sodium ion diffusion barrier, revealing the high Na intercalation concentration in layered CrN_2. Besides, the formation energy and phonon spectrum were also calculated to analyze the stability of layered CrN_2. Plus, we also calculated the charge transfer and electronic properties. All of the results show that layered CrN_2 is a desirable electrode SIBs with good electrochemical performance.

2. Computational methods

We build our calculations on Vienna *ab initio* simulation package (VASP),[34] a first-principles calculation software package based on density functional theory (DFT), and adopt the projected augmented wave (PAW)[35] method to depict the interaction between ion nuclei and valence electrons. Besides, the electron exchange-correlation is described *via* Perdew–Burke–Ernzerhof (PBE) functional in generalized gradient approximation (GGA).[36] The long-range van der Waals interactions are depicted exactly with the DFT-D3 correction method.[37,38] In this study, the cut-off energy of plane wave base expansion is set to 500 eV. The structural relaxation is geometrically optimized *via* the conjugate gradient (CG) method until the force on each atom is less than 0.01 eV $Å^{-1}$ and reaches the energy convergence standard of 10^{-6} eV. For Brillouin zone sampling, the reciprocal space of the Brillouin zone is integrated with 18 × 18 × 6 M-P grid *k* points. Differential charge density and Bader charge analysis are used to show and measure charge transfer on atoms respectively. Band structure and density of states calculations are applied to analyze the electronic properties of materials. In the calculation of energy band structure, 140 *k* points are selected along the line of high symmetry points in reciprocal space. Spin polarization is taken into account in all calculations since the system contains magnetic 3d transition metal elements. Besides, the phonon spectrum is calculated *via* phonopy code.[39]

To investigate the stability of materials, we compute both the formation energy and phonon spectrum of materials. The formation energy E_{form} is defined as the formula (1):

$$E_{form} = (E_{NaMX_2} - \mu_{Na} - \mu_M - 2\mu_X)/4 \quad (1)$$

where the E_{NaMX2} represents the total energy of a $NaMX_2$ unit cell, and the μ_{Na}, μ_M and μ_X are the chemical potential of Na, M and X atoms, respectively.

To study the diffusion properties of sodium ions in MX_2, a 3 × 3 × 1 supercell consisting of 18 M atoms and 36 X atoms is used, and a 6 × 6 × 6 *K*-point grid is adopted. The diffusion performance of sodium in MX_2 is calculated through the climbing image nudge elastic band (CI-NEB) method.[40,41] Specifically, a series of intermediate images are inserted between the optimized initial structure and the final structure, and then each image finds the lowest potential energy configuration along the reaction path. The energy and force convergence criteria of diffusion calculation are set to be 10^{-5} eV and 0.02 eV $Å^{-1}$ respectively to improve the calculation efficiency. This method can accurately locate the diffusion path of the lowest energy and the diffusion barrier.

The theoretical capacity[42] *C* is calculated according to formula (2):

$$C = \frac{nF}{3.6M} \quad (2)$$

where *n* is the valence electron number of sodium (here $n = 1$), *F* is the Faraday constant (96485 C mol^{-1}), and *M* is the relative molecular mass of the MX_2 molecular formula unit.

The equation for deriving voltage[43] *V* is expressed as:

$$V = -(E_{Nax2CrN_2} - E_{Nax1CrN_2} - (x2 - x1)E_{Na})/(x2 - x1)e \quad (3)$$

where $E_{Nax2CrN_2}$ and $E_{Nax2CrN_2}$ represent the total energy of $Na_{x1}CrN_2$ and $Na_{x2}CrN_2$ respectively, E_{Na} represents the energy of a single sodium atom in metal sodium, and *e* is the electric quantity carried by every single electron (1.6×10^{-19} C).

3. Results and discussion

3.1. Screening of materials

There is a sandwich-like X–M–X structure similar to TMDs in MX_2, in which each M atom is coordinated with six X atoms to form a triangular prism or octahedral coordination configuration, and each X atom is coordinated with three M atoms. Due to the difference in the coordination configuration of M and the stacking period along the *c*-axis, the materials have several different configurations, among which 1T-phase and 2H-phase are the most common structural configurations in this type of material.[44] In the 2H-phase, each M atom and six X atoms form a triangular prism, and the MX_2 layer is stacked in AB order (as is shown in Fig. 1a). In the 1T-phase, each M atom is surrounded by six X atoms to form an octahedral coordination configuration, and the MX_2 layer is stacked in AA order (as is shown in Fig. 1b). Therefore, a 1 × 1 × 2 supercell of 1T-phase

and 1 × 1 × 1 unit-cell of 2H-phase were calculated, both of which have 2 MX_2 layers containing 2 M atoms and 4 X atoms.

To study the structural properties of different phases, we have fully optimized all 1T- and 2H-phase MX_2, and the fully optimized structures of these MX_2 are shown in Fig. S1,† and the lattice parameters of all MX_2 are shown in Table S1.† The cell parameters of 2H-phase VN_2 we calculated are in agreement with those of theoretically reported H-phase VN_2 monolayer,[45] as is shown in Table S2.† The results indicate that almost all 2H-phase MX_2 maintained layered structures well, but most of 1T phase structures tend to collapse or slope, 1T-MC_2 in particular. Fig. 1c gives the interlayer spacing of all 1T- and 2H-phase MX_2. It is shown that most of MX_2 has an interlayer spacing from 1.4 Å to 2.7 Å. However, 1T-phase TiC_2, VC_2, MnC_2, FeC_2 and 2H-phase TiC_2, VC_2 have no interlayer spacing because they have formed compounds. From the comparison of interlayer spacing between 1T- and 2H-phase MX_2, it is obvious that most 2H-phase MX_2 have larger interlayer spacing than 1T-phase. Larger interlayer spacing is beneficial to intercalation and diffusion for Na. Therefore, 2H-phase MX_2 is fitter to serve as electrode materials.

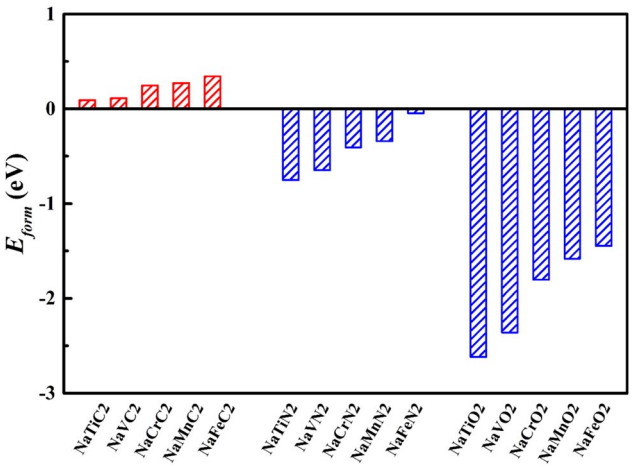

Fig. 2 The formation energy of all 2H-phase $NaMX_2$ systems (M = Ti, V, Cr, Mn and Fe; X = C, N and O).

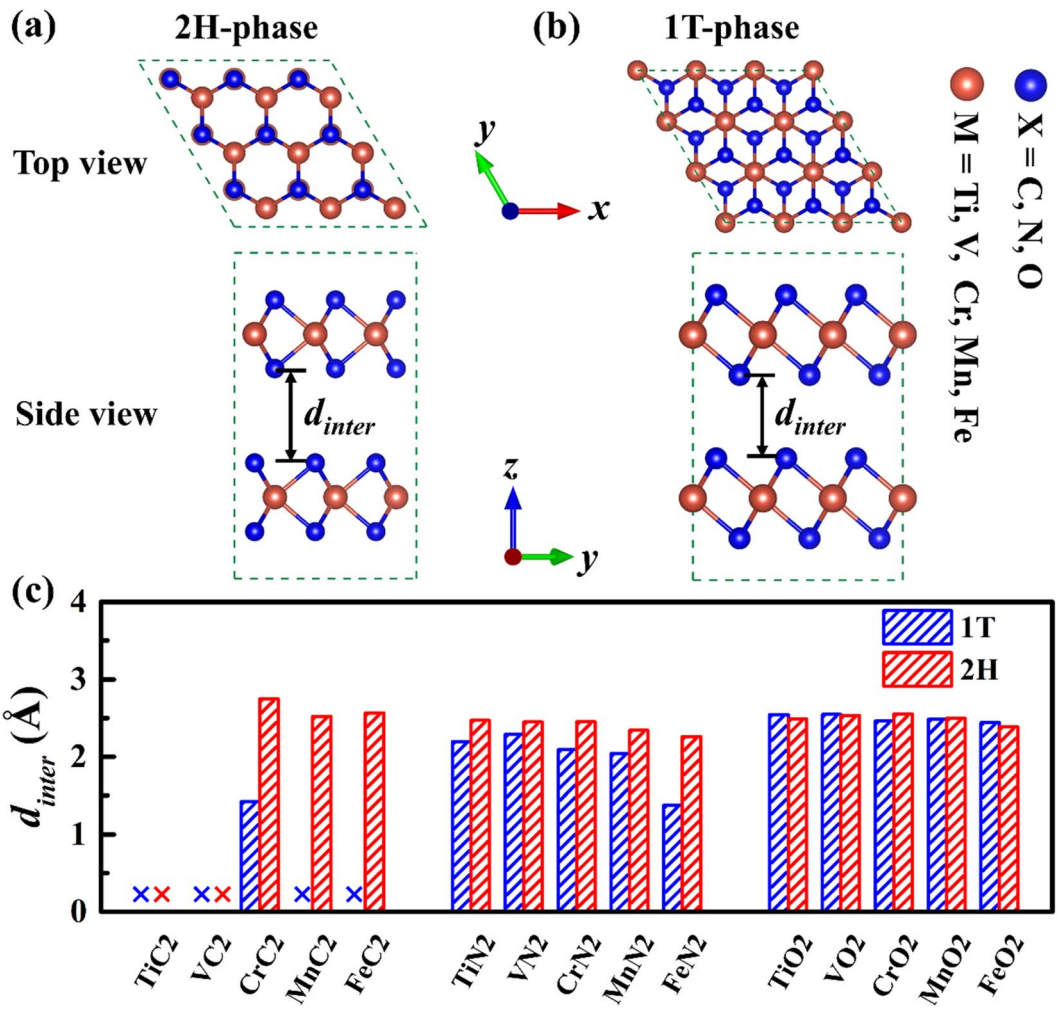

Fig. 1 The top and side views of 2H-phase (a) and 1T-phase (b) MX_2 structure respectively (brown balls represent M atoms (M = Ti, V, Cr, Mn and Fe), and blue balls represent X atoms (X = C, N and O)). (c) The interlayer spacing of all 1T- and 2H-phase MX_2.

To ascertain the energy stability of the $NaMX_2$ structure, we have computed the formation energy of all 2H-phase $NaMX_2$ systems (as is shown in Fig. 2). The results show that the corresponding nitrides and oxides have a negative formation energy while carbides have a positive formation energy, which indicates the $NaMN_2$ and $NaMO_2$ systems enjoy better stability than $NaMC_2$. Better stability is beneficial to the preparation of materials. Therefore, N and O are the selected anions for its compounds whose formation energy is lower than C. Negative formation energy suggests that better cycling stability can be expected for N- and O-based compounds when they are used as the electrode materials for SIBs.

Theoretical capacity, as we know, is an important factor in the applications of electrode materials, so we have calculated the theoretical capacity of different MX_2 (M = Ti, V, Cr, Mn and Fe; X = N and O) materials, and the results are shown in Fig. 3. Benefiting from the lighter relative atomic masses of 3d transition metals and 2p non-metallic elements, all MX_2 (M = Ti, V, Cr, Mn and Fe; X = N and O) materials possess a higher theoretical capacity (305–353 mA h g^{-1}). Among them, CrN_2 has a theoretical capacity of 335 mA h g^{-1}, which is much larger than traditional oxide materials[46] and polyanionic compound materials[47] and is nearly twice that of MoS_2 (167 mA h g^{-1}).[48]

Ion diffusion is a key issue in the application of electrode materials for sodium-ion batteries. The rapid sodium diffusion determines the high-rate performance of the battery, ensuring the battery a high charge and discharge rate.[49,50] Therefore, we have studied the migration properties of 2H-phase MX_2 (M = Ti, V, Cr, Mn and Fe; X = C, N and O) materials. It is found that the most stable intercalation site of sodium is an octahedral gap (O1 or O2), as is shown in Fig. 3a and b. And according to the previous reporting on the migration of TMDs materials,[51] the migration path of sodium is between two adjacent octahedral interstitial sites through tetrahedral interstitial sites (O1–T–O2), as is shown in Fig. 4a and b. The diffusion barrier of all Na in MX_2 (M = Ti, V, Cr, Mn and Fe; X = N and O) are shown in Fig. 4c. And the diffusion energy profile along the diffusion path is shown in Fig. 5a and S2.† It is shown that all of the materials have a lower barrier. In particular, the diffusion barrier of sodium ions in CrN_2 is the lowest, about 0.49 eV. Thus, CrN_2 as an electrode material of sodium-ion battery boasts satisfactory rate performance.

3.2. Properties of CrN_2 as an electrode material

Due to the lowest diffusion barrier of CrN_2 (0.49 eV), lower than CrC_2 (0.7 eV) and CrO_2 (0.52 eV), it was chosen as the best electrode material for SIBs (as is shown in Fig. 5a). To better understand the dynamic stability of CrN_2 materials, we have calculated the phonon spectrum. There is no virtual frequency in the phonon spectrum (as is shown in Fig. 5b), which indicates CrN_2 is dynamically stable. Thus, CrN_2 possesses not only thermal stability (see Fig. 2) but also dynamical stability, which indicates a good cycling stability when it is used as electrode material for SIBs.

As intercalation energy is a crucial parameter for measuring the level of difficulty in inserting sodium ions into the materials, we have calculated the intercalation energy of sodium inserting CrN_2 at different sodium concentrations. It suggests that CrN_2 has a large negative intercalation energy indicating the feasibility of inserting Na into it (see Fig. S3†). The most stable configurations of Na_xCrN_2 (x ranges from 0 to 1) at different sodium concentrations are shown in Fig. S4 in the ESI.† Fig. 6a shows the calculated intercalation energy at different concentrations. It suggests that the intercalation energy initially decreases at the concentration from 0.00 to 0.33 as the effective interaction of the sodium ions is attractive, and then increases at the concentration from 0.33 to 1.00 when the

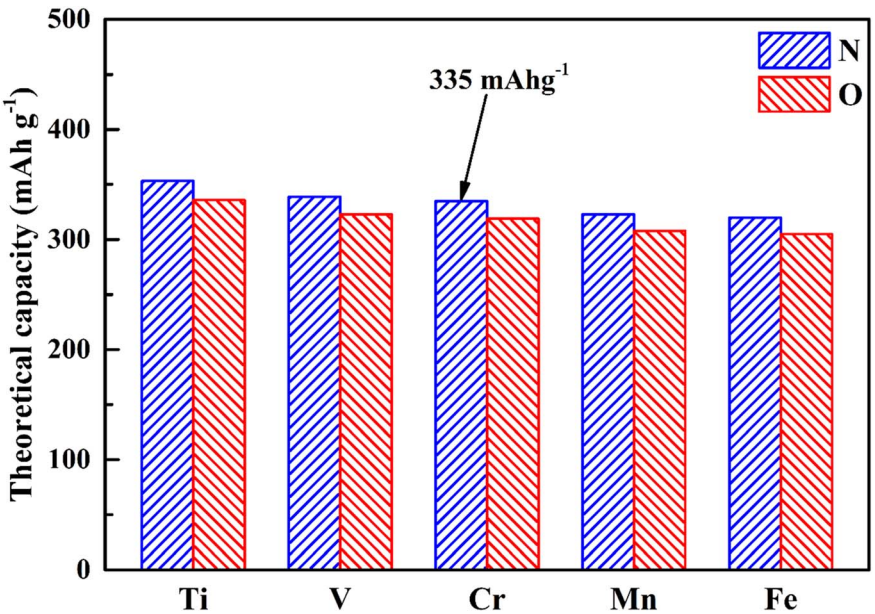

Fig. 3 The theoretical capacity of MX_2 (M = Ti, V, Cr, Mn and Fe; X = N and O) materials.

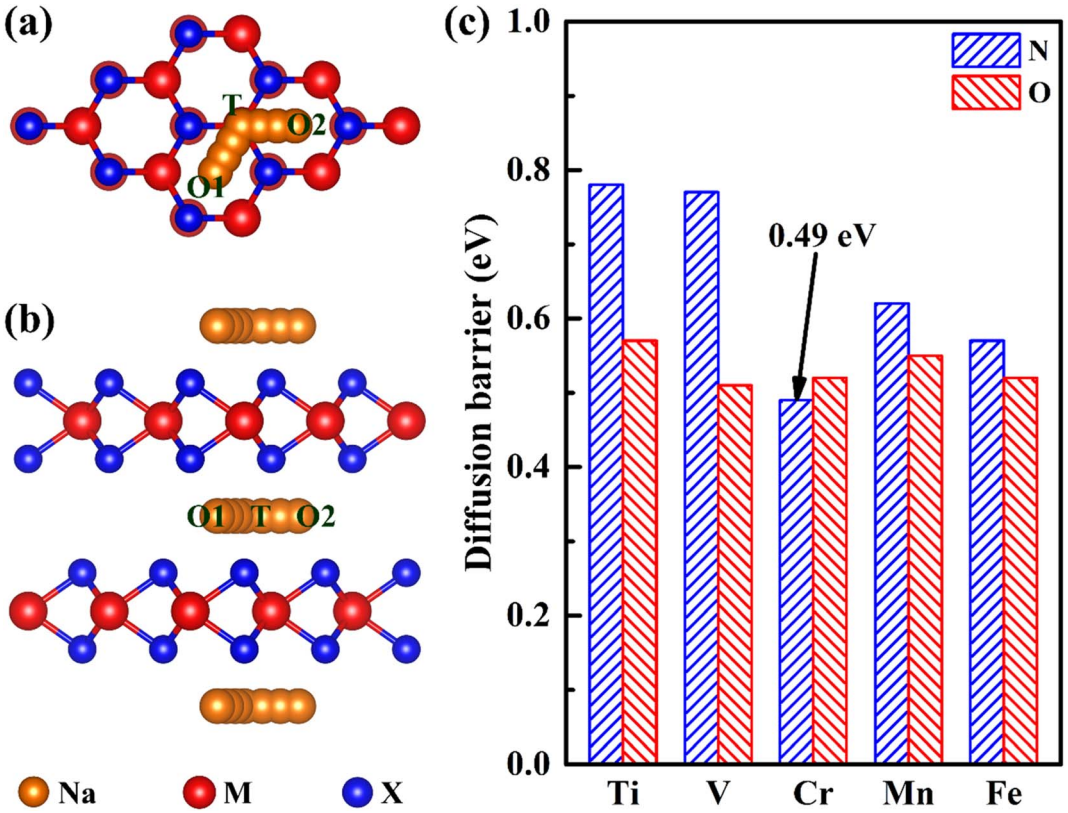

Fig. 4 The top view (a) and side view (b) of diffusion paths (O1–T–O2) of sodium ion in MnX_2 and the most stable adsorption sites (O1 or O2) of sodium ions in 2H-phase MnX_2 (light brown balls represent sodium, red balls represent M atoms (M = Ti, V, Cr, Mn and Fe), and blue balls represent X atoms (X = N and O)). (c) The diffusion barrier of sodium ions in 2H-phase MX_2 materials.

effective interaction of the sodium ions becomes repulsive. When sodium reaches the maximum concentration of 1, its intercalation energy achieves the maximum value of −3.4 eV. Overall, negative intercalation energy is conducive to sodium ion intercalated. And volume expansion rate of sodium in the process of embedding CrN_2 is less than 10%, which is beneficial to the cyclic stability of the material.

As voltage is also a critical parameter for electrode materials, we have calculated the voltage of CrN_2 under different sodium concentrations. The calculated voltage is a function of sodium concentration in CrN_2 (see Fig. 6b). It shows CrN_2 boasts a high voltage window of about 3.1–3.8 V. Such a high voltage makes it ideal for cathode materials. When $x1 = 0$ and $x2 = 1$, the computed voltage (3.4 V) is the open-circuit voltage. Combining

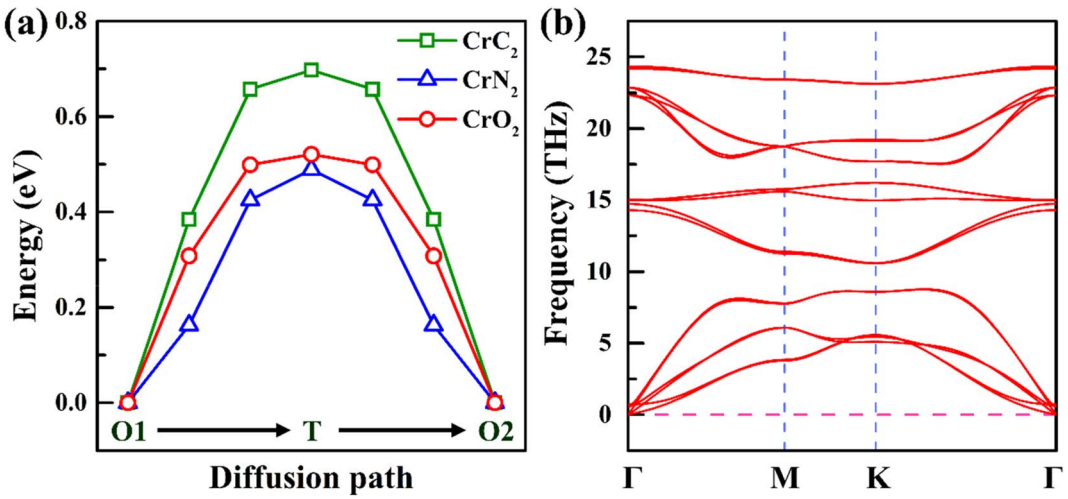

Fig. 5 (a) Energy profile of Na diffusion along the diffusion path in 2H-phase CrX_2 (X = C, N, O). (b) Phonon spectrum of 2H-phase CrN_2.

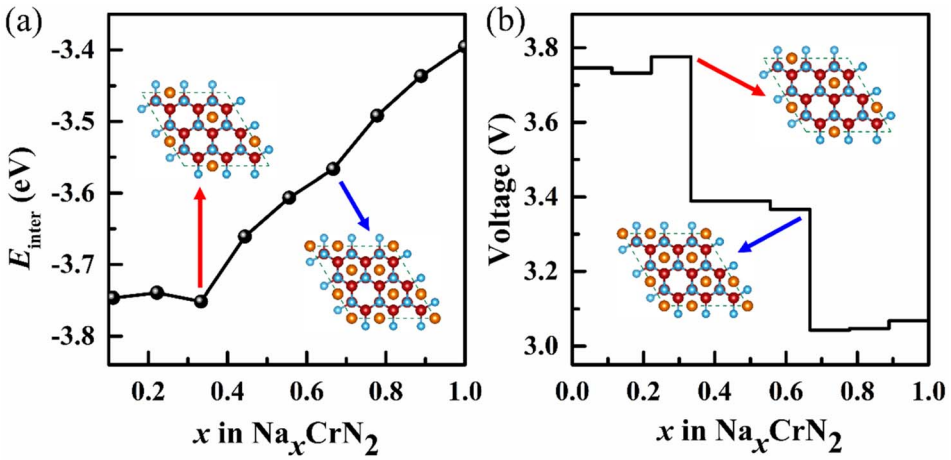

Fig. 6 (a) Intercalation energy (E_{inter}) of Na_xCrN_2 ($x = 0$–1) under different sodium concentrations. (b) Voltage profile under different sodium concentrations. Insets represent the intercalation configurations for Na_xCrN_2 ($x = 0.33$ and $x = 0.67$), respectively (red and blue arrow point to $Na_{0.33}CrN_2$ and $Na_{0.67}CrN_2$, respectively) (for more configurations at all sodium concentrations please see Fig. S4 in the ESI†).

the open-circuit voltage and theoretical capacity, the CrN_2 has a high energy density of 1139 W h kg^{-1}, which is much higher than that of traditional cathode materials, like transition metal oxides (less than 800 W h kg^{-1}), polyanionic compounds (no more than 500 W h kg^{-1}) and Prussian blue analogs (about 500 W h kg^{-1}).[52]

To reveal the mechanism of sodium ion intercalation, we have examined the charge transfer after sodium ion intercalated. The differential charge density is shown in Fig. S5 in the ESI.† The yellow electron-rich regions on the nitrogen atom and the cyan electron-deficient regions around the sodium atom indicate that the charge has been transferred from the sodium

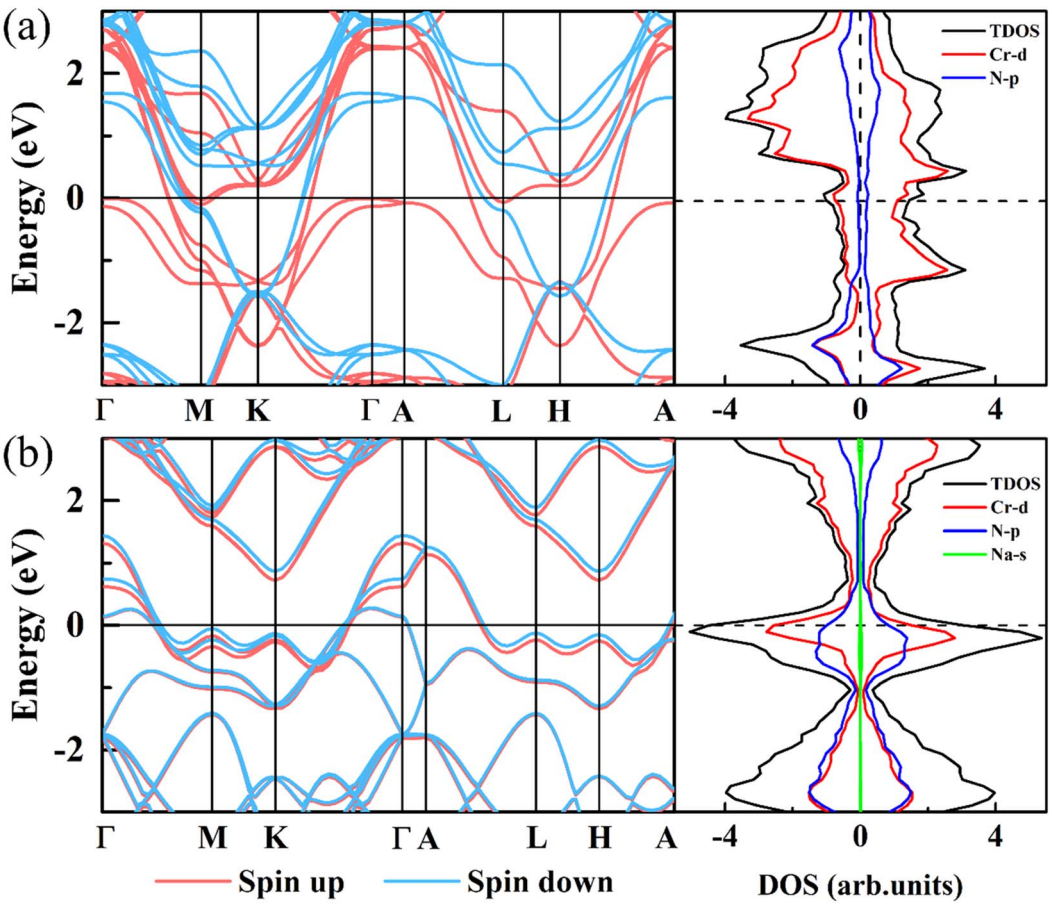

Fig. 7 Band structure and density of states of 2H-phase CrN_2 (a) and 2H-phase $NaCrN_2$ (b), respectively. The Fermi level is set to zero.

atom to the CrN_2 substrate. Bader charge analysis calculated the number of charge transfers in great detail. The results show that the sodium atom transfer 0.73 electrons and the electrons are mainly transferred from Na to the N atom. Charge transfer means that sodium is in a cationic state, and the Na–N bond has obvious ionic characteristics. In addition, the strong sodium–nitrogen interaction further shows that sodium can be stably embedded into CrN_2.

To further study the electronic structure of CrN_2, we have calculated band structures and density of states, which are shown in Fig. 7. In band structure, it is shown that the CrN_2 material exhibits metallic features both before and after sodium-ion intercalation, which endows it with a fast charge and discharge rate. According to the density of states near the Fermi level, the CrN_2 exhibits ferromagnetism before sodium-ion intercalation in TDOS, which is mainly contributed by the Cr-d orbital electrons in PDOS. The fully sodiated state of CrN_2 presents non-magnetic, and the density of N-p orbital states near the Fermi level is significantly enhanced, and the hybridization of Cr-d orbital and N-p orbital is enhanced, improving the cycle stability of the CrN_2 material. In addition, the electrical double-layered structure induced by strong charge transfer between sodium and nitrogen enables the sodium-ion diffusion barrier to be reduced greatly.

4. Conclusions

In this paper, we systematically studied the theoretical capacity and ion diffusion barrier in a new type of layered bulk transition meta compounds, named MX_2 (M = Ti, V, Cr, Mn, Fe; X = C, N, O). Our results show that most of these layered MX_2 materials possess a high theoretical capacity of over 300 mA h g^{-1}. In particular, 2H-phase layered bulk CrN_2 possesses a proper theoretical capacity (335 mA h g^{-1}) and a desirable sodium ion diffusion barrier (0.49 eV). In addition, the layered CrN_2 has both good thermal and dynamical stability. Importantly, the results of charge transfer and electronic properties lead to the high voltage platform from 3.1 to 3.8 V and extraordinary electrochemical performance of layered CrN_2. Moreover, CrN_2 boasts a high energy density of 1139 W h kg^{-1} thanks to its high open-circuit voltage (3.4 V) combined with high theoretical capacity. Our predicted 2H-phase layered transition-metal nitrides enjoy great potential to be ideal candidates for SIBs cathode materials.

Conflicts of interest

There are no conflicts to declare.

Acknowledgements

This work is supported by the National Natural Science Foundation of China (No. 11772285, 11774298, 11604278). Research Foundation of Xiangtan University (21QDZ39) and Education Department of Hunan Province (21C0093).

Notes and references

1 J. Y. Hwang, S. T. Myung and Y. K. Sun, *Chem. Soc. Rev.*, 2017, **46**, 3529–3614.
2 Q. Bai, L. F. Yang, H. L. Chen and Y. F. Mo, *Adv. Energy Mater.*, 2018, **8**, 1702998.
3 X. Xiang, K. Zhang and J. Chen, *Adv. Mater.*, 2015, **27**, 5343–5364.
4 L. L. Wong, H. Chen and S. Adams, *Phys. Chem. Chem. Phys.*, 2017, **19**, 7506–7523.
5 J. Xiao, X. Li, K. Tang, D. Wang, M. Long, H. Gao, W. Chen, C. Liu, H. Liu and G. Wang, *Mater. Chem. Front.*, 2021, **5**, 3735–3764.
6 R. J. Clément, D. S. Middlemiss, I. D. Seymour, A. J. Ilott and C. P. Grey, *Chem. Mater.*, 2016, **28**, 8228–8239.
7 Y. J. Fang, X. Y. Yu and X. W. Lou, *Angew. Chem. Int., Ed.*, 2017, **56**, 5801–5805.
8 H. D. Luong, V. A. Dinh, H. Momida and T. Oguchi, *Phys. Chem. Chem. Phys.*, 2020, **22**, 18219–18228.
9 M. Sathiya, Q. Jacquet, M.-L. Doublet, O. M. Karakulina, J. Hadermann and J.-M. Tarascon, *Adv. Energy Mater.*, 2018, **8**, 1702599.
10 H. Xia, X. Zhu, J. Liu, Q. Liu, S. Lan, Q. Zhang, X. Liu, J. K. Seo, T. Chen, L. Gu and Y. S. Meng, *Nat. Commun.*, 2018, **9**, 5100.
11 F. Bianchini, H. Fjellvåg and P. Vajeeston, *Mater. Chem. Phys.*, 2018, **219**, 212–221.
12 B. Senthilkumar, K. V. Sankar, L. Vasylechko, Y.-S. Lee and R. K. Selvan, *RSC Adv.*, 2014, **4**, 53192–53200.
13 Q. Ni, Y. Bai, F. Wu and C. Wu, *Adv. Sci.*, 2017, **4**, 1600275.
14 B.-K. Zou, Y. Shao, Z.-Y. Qiang, J.-Y. Liao, Z.-F. Tang and C.-H. Chen, *J. Power Sources*, 2016, **336**, 231–239.
15 A. Gutierrez, S. Kim, T. T. Fister and C. S. Johnson, *ACS Appl. Mater. Interfaces*, 2017, **9**, 4391–4396.
16 B.-M. Zhang, C.-B. Zhang, H. Zhang, Y.-X. Hu, Y.-S. Zhang, C. Lu, J. Li, L.-B. Kong and M.-C. Liu, *Appl. Surf. Sci.*, 2020, **513**, 145826.
17 S. Fan, X. Zou, H. Du, L. Gan, C. Xu, W. Lv, Y.-B. He, Q.-H. Yang, F. Kang and J. Li, *J. Phys. Chem. C*, 2017, **121**, 13599–13605.
18 D. B. Putungan and J. L. Kuo, *Phys. Chem. Chem. Phys.*, 2021, **23**, 19811–19818.
19 Q. Su, X. Cao, X. Kong, Y. Wang, C. Peng, J. Chen, B. Yin, J. Shi, S. Liang and A. Pan, *Electrochim. Acta*, 2018, **292**, 339–346.
20 H. Wang, X. Lan, D. Jiang, Y. Zhang, H. Zhong, Z. Zhang and Y. Jiang, *J. Power Sources*, 2015, **283**, 187–194.
21 M. Feng, M. Zhang, H. Zhang, X. Liu and H. Feng, *Carbon*, 2019, **153**, 217–224.
22 Z. Liu, H. Deng, S. Zhang, W. Hu and F. Gao, *J. Mater. Chem. A*, 2018, **6**, 3171–3180.
23 X. J. Ye, J. Xu, Y. D. Guo and C. S. Liu, *Phys. Chem. Chem. Phys.*, 2021, **23**, 4386–4393.
24 J. Zeng, J. Huang, J. Liu, T. Xie, C. Peng, Y. Lu, P. Lu, R. Zhang and J. Min, *Carbon*, 2019, **154**, 24–32.
25 X. Zhao, X. Zhang, D. Wu, H. Zhang, F. Ding and Z. Zhou, *J. Mater. Chem. A*, 2016, **4**, 16606–16611.

26 N. Khossossi, W. Luo, Z. Haman, D. Singh, I. Essaoudi, A. Ainane and R. Ahuja, *Nano Energy*, 2022, **96**, 107066.
27 K. Niwa, T. Yamamoto, T. Sasaki and M. Hasegawa, *Phys. Rev. Mater.*, 2019, **3**, 053601.
28 F. Kawamura, H. Yusa and T. Taniguchi, *Appl. Phys. Lett.*, 2012, **100**, 251910.
29 T. Chen, E. Castanon, J. G. Gigax, H. Kim, R. Balerio, J. Fan, F. A. Garner and L. Shao, *Nucl. Instrum. Methods Phys. Res., Sect. B*, 2019, **451**, 10–13.
30 Z. Zhao, K. Bao, F. Tian, D. Duan, B. Liu and T. Cui, *Phys. Rev. B*, 2016, **93**, 214104.
31 X. Zhang, Z. Yu, S.-S. Wang, S. Guan, H. Y. Yang, Y. Yao and S. A. Yang, *J. Mater. Chem. A*, 2016, **4**, 15224–15231.
32 J. Xu, D. Wang, Y. Liu, R. Lian, X. Gao, G. Chen and Y. Wei, *J. Mater. Chem. A*, 2019, **7**, 26858–26866.
33 G. Liu, S. Xu, L. Wu, J. Zhang, Q. Wang and P. Lu, *Mater. Chem. Phys.*, 2020, **250**, 123028.
34 G. Kresse and J. Furthmüller, *Phys. Rev. B: Condens. Matter Mater. Phys.*, 1996, **54**, 11169–11186.
35 P. E. Blöchl, *Phys. Rev. B: Condens. Matter Mater. Phys.*, 1994, **50**, 17953–17979.
36 J. P. Perdew, K. Burke and M. Ernzerhof, *Phys. Rev. Lett.*, 1996, **77**, 3865–3868.
37 W. Hujo and S. Grimme, *J. Chem. Theory Comput.*, 2011, **7**, 3866–3871.
38 S. Grimme, S. Ehrlich and L. Goerigk, *J. Comput. Chem.*, 2011, **32**, 1456–1465.
39 A. Togo and I. Tanaka, *Scr. Mater.*, 2015, **108**, 1–5.
40 G. Henkelman and H. Jónsson, *J. Chem. Phys.*, 2000, **113**, 9978–9985.
41 G. Henkelman, B. P. Uberuaga and H. Jónsson, *J. Chem. Phys.*, 2000, **113**, 9901–9904.
42 D. Datta, J. Li and V. B. Shenoy, *ACS Appl. Mater. Interfaces*, 2014, **6**, 1788–1795.
43 I. A. Courtney, J. S. Tse, O. Mao, J. Hafner and J. R. Dahn, *Phys. Rev. B: Condens. Matter Mater. Phys.*, 1998, **58**, 15583–15588.
44 Y. Wang, J. Xiao, H. Zhu, Y. Li, Y. Alsaid, K. Y. Fong, Y. Zhou, S. Wang, W. Shi, Y. Wang, A. Zettl, E. J. Reed and X. Zhang, *Nature*, 2017, **550**, 487–491.
45 Y. Dong, Z. Tang, P. Liang, H. Wan, H. Wang, L. Wang, H. Shu and D. Chao, *J. Colloid Interfaces Sci.*, 2021, **593**, 51–58.
46 Q. N. Liu, Z. Hu, M. Z. Chen, C. Zou, H. L. Jin, S. Wang, S. L. Chou, Y. Liu and S. X. Dou, *Adv. Funct. Mater.*, 2020, **30**, 1909530.
47 S. Chakraborty, A. Banerjee, T. Watcharatharapong, R. B. Araujo and R. Ahuja, *J. Phys.:Condens. Matter*, 2018, **30**, 283003.
48 J. C. Su, Y. Pei, Z. H. Yang and X. Y. Wang, *RSC Adv.*, 2014, **4**, 43183–43188.
49 Y. Jing, J. Liu, Z. P. Zhou, J. Zhang and Y. F. Li, *J. Phys. Chem. C*, 2019, **123**, 26803–26811.
50 J. Liu, M. Qiao, X. Zhu, Y. Jing and Y. Li, *RSC Adv.*, 2019, **9**, 15536–15541.
51 M. Mortazavi, C. Wang, J. K. Deng, V. B. Shenoy and N. V. Medhekar, *J. Power Sources*, 2014, **268**, 279–286.
52 Y. C. Lyu, Y. C. Liu, Z. E. Yu, N. Su, Y. Liu, W. X. Li, Q. Li, B. K. Guo and B. Liu, *Sustainable Mater. Technol.*, 2019, **21**, e00098.